Surface & Coatings Technology 494 (2024) 131378

Contents lists available at ScienceDirect

Surface & Coatings Technology

journal homepage: www.elsevier.com/locate/surfcoat

Enhancing geometric integrity and surface hardness of SLM-printed Ti-6Al-4V components with support structures and laser nitriding

Weijie Xie [a,b], Conall Kirk [b], Amal Rejee [b], Hau-Chung Man [a,c,*], Chi-Wai Chan [b,**]

[a] Department of Industrial and Systems Engineering, The Hong Kong Polytechnic University, Hong Kong, China
[b] School of Mechanical and Aerospace Engineering, Queen's University, Belfast BT9 5AH, UK
[c] Research Institute for Advanced Manufacturing, The Hong Kong Polytechnic University, Hong Kong, China

ARTICLE INFO

Keywords:
Selective laser melting (SLM)
Support structures
Laser Nitriding
Surface hardness

ABSTRACT

This study investigated the effect of support structure and post-processing surface nitriding on high aspect ratio Ti-6Al-4V components fabricated using Selective Laser Melting (SLM). It examined changes in geometric integrity, porosity, and mechanical properties. Samples were printed without support structures (S1) and with support structures (S2). After SLM printing, both samples underwent open-air laser nitriding at duty cycles (DC) ranging from 50 % to 100 %, aiming to create crack-free nitride layers to increase surface hardness. The results indicated that support structures effectively mitigate thermal-induced deformation, with S2 exhibiting minimal warping and closer adherence to design specifications than S1. Although S2 showed increased porosity as revealed by X-ray Computed Tomography (XCT), its refined microstructure contributed to increased hardness. Optical Microscope and Scanning Electron Microscope (SEM) analyses demonstrated that laser nitriding at a 50 % duty cycle produced uniform, crack-free titanium nitride (TiN) layers. Vickers hardness tests revealed a significant enhancement in the surface hardness of both laser-nitrided samples, with S2 displaying finer TiN dendrites that further improved its surface hardness. The use of support structures was found to be effective in achieving a more uniform microstructure and enhanced hardness in the nitride layer.

1. Introduction

Selective Laser Melting (SLM) is an additive manufacturing technique that allows rapid fabrication of metal parts with complex geometries. This layer-by-layer process not only enables the creation of intricate designs but also significantly reduces material wastage, presenting a greener manufacturing approach. By fine-tuning the SLM process parameters (e.g., laser power, scanning strategy, focus position, layer thickness, etc.), one can tailor the material properties to meet specific requirements, enhancing the functionality and performance of the fabricated components [1,2]. Besides, Ti-6Al-4V, commonly known as Ti64, is an alpha + beta titanium alloy renowned for its excellent strength-to-weight ratio, good mechanical strength, biocompatibility, and superior corrosion resistance.

Ensuring geometric integrity is crucial in the SLM printing of Ti64 components, particularly those with high aspect ratios. This is due to the complex and non-uniform nature of heat distribution and material solidification processes [3], which often lead to deformation. One specific challenge is the deformation that occurs when components are detached from the substrate. This deformation is usually a result of residual stresses and the thermal gradient induced during the cooling process. When these components are separated from the substrate through wire cutting, the stresses can cause them to warp or distort.

Support structures are important in SLM printing. They provide mechanical support to complex features and overhangs, reducing the risks of deformation during printing and post-processing to maintain part quality. Thomas et al. [4] reported that support structures are necessary for fabricating overhanging features inclined at angles up to 45°, which help in preventing the collapse of samples due to gravity. Gan et al. [5] highlighted that support structures facilitate the removal of printed parts from the substrate, thereby minimising damage during detachment. They also found that the design of the support structure affects the levelness and overall quality of the built parts. Xiaohui et al. [6] found that support structures can reduce residual stress by promoting more uniform cooling and solidification rates across the parts. However, Kurzynowski et al. [7] identified a potential drawback that the

* Correspondence to: H-C Man, Department of Industrial and Systems Engineering, The Hong Kong Polytechnic University, Hong Kong, China.
** Corresponding author.
E-mail addresses: hc.man@polyu.edu.hk (H.-C. Man), c.w.chan@qub.ac.uk (C.-W. Chan).

https://doi.org/10.1016/j.surfcoat.2024.131378
Received 22 July 2024; Received in revised form 9 September 2024; Accepted 15 September 2024
Available online 18 September 2024

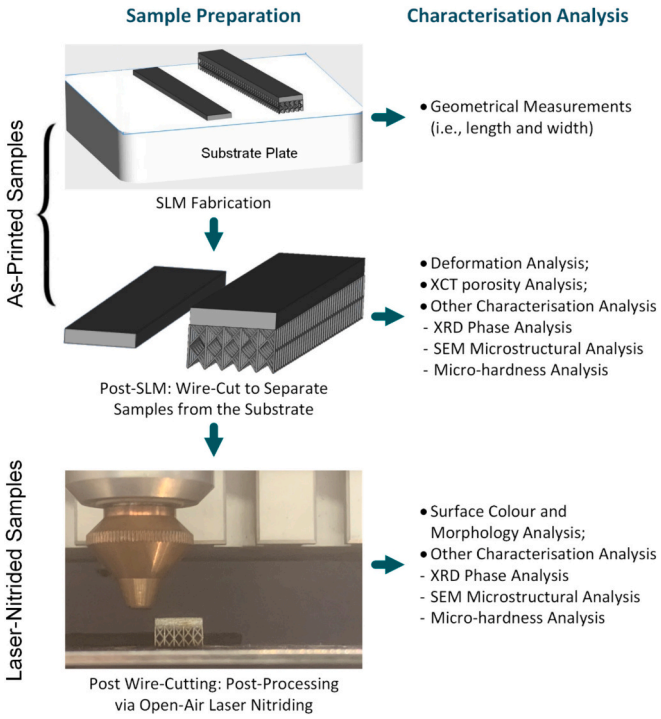

Fig. 1. Experimental workflow for sample preparation and characterisation.

use of support structures can increase porosity in printed parts. This issue can be mitigated by incorporating intermediate layers between the support and the samples, which act as heat sinks.

Porosity is a well-known challenge that compromises the integrity and performance of SLM-fabricated parts, adversely affecting mechanical strength and overall durability. Increased porosity typically results in reduced mechanical strength. Research by Palmeri et al. [8] illustrates how varying build orientations affect porosity and subsequently affect tensile strength. Cui et al. [9] found that porosity significantly decreases the elastic limit of Ti64. Jonathan et al. [10] investigated the impact of scanning strategy (e.g., laser spot path) on porosity, discovering that pores predominantly occur at the overlaps between laser scans. Punit et al. [11] reported that porosity is a major contributor to the poor fracture toughness and fatigue resistance in Ti64. Despite these findings, the specific impact of support structures on porosity in high aspect ratio Ti64 components remains under-explored, highlighting a research gap for further investigation.

Post-processing surface treatment serves as an important step following the SLM process, targeting both residual stress and porosity at the surface of the components. It also focuses on enhancing surface properties. Laser nitriding has emerged as an effective surface treatment technique for enhancing surface hardness, wear resistance, and corrosion resistance of SLM-fabricated Ti64 components. However, while

Table 1
Chemical composition of Ti64 powder (all results in weight%).

Al	Ti	V	O	Fe
5.29	Balance	3.88	0.95	1.02

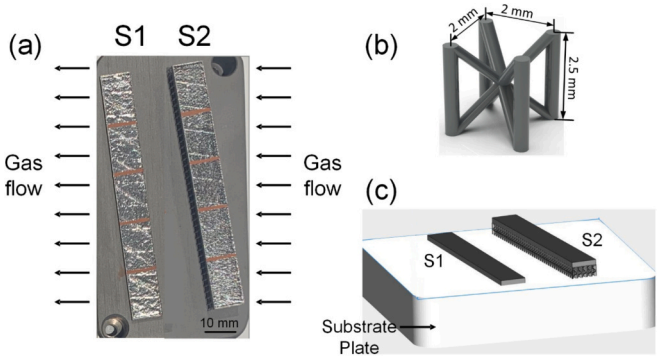

Fig. 3. (a) Overview of as-printed samples: S1 and S2; (b) Single unit of support structure used in S2; it is repeated to provide full support for the sample (80 mm × 10 mm) in two layers, resulting in a total support height of 5 mm; (c) CAD model of S1 and S2.

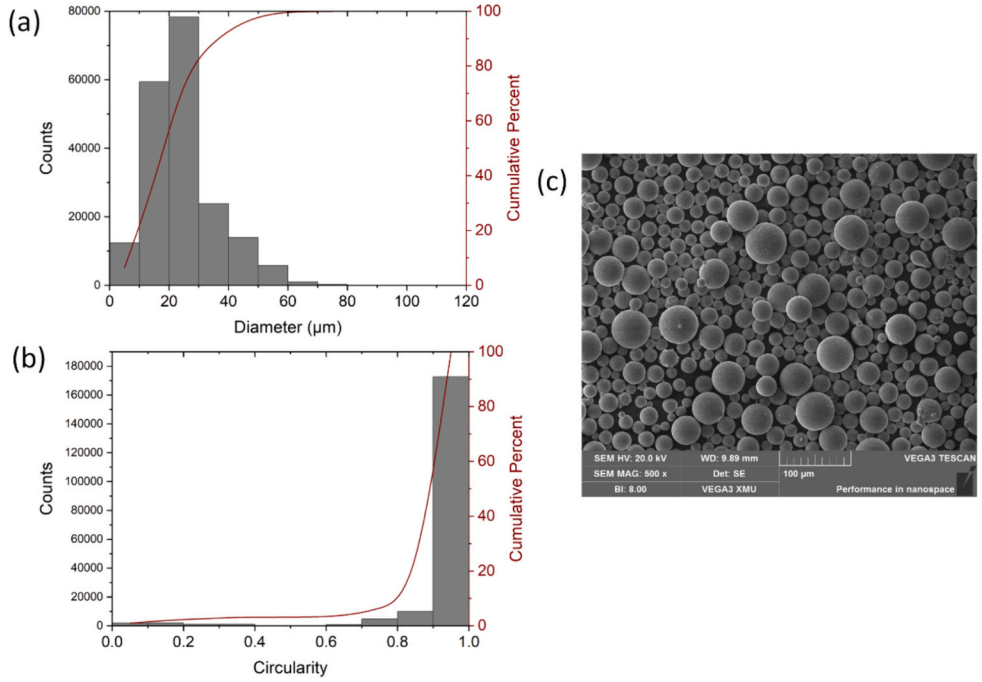

Fig. 2. Analysis of Ti64 powder characteristics: (a) particle size distribution; (b) particle circularity; (c) morphology via SEM.

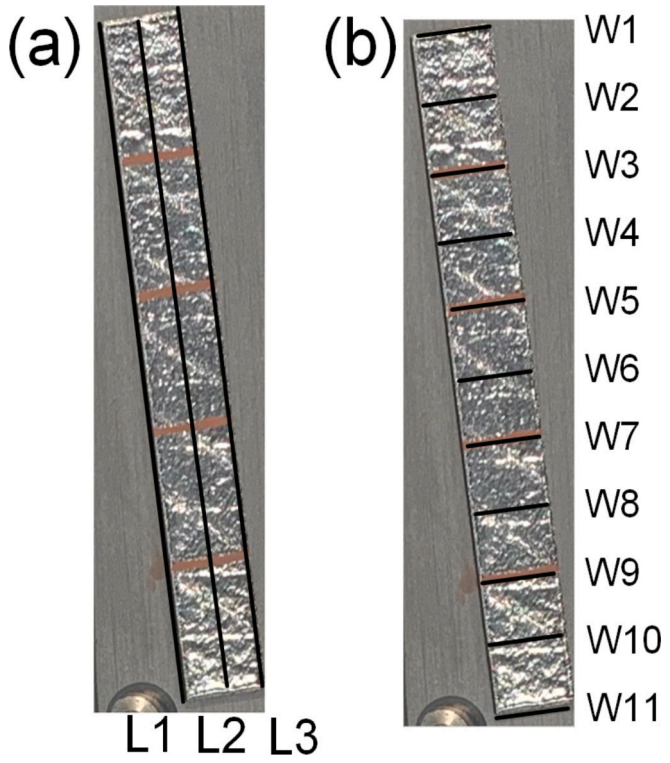

Fig. 4. Schematic representation illustrating geometrical measurements: (a) length; (b) width.

Table 2
Designations of samples subjected to various SLM and laser nitriding conditions.

Denotations	Support structure	Duty cycle (DC in laser nitriding)
S1DC50	No	50 %
S1DC75	No	75 %
S1DC100	No	100 %
S2DC50	Yes	50 %
S2DC75	Yes	75 %
S2DC100	Yes	100 %

promising in forming a TiN layer for improved properties, laser nitriding presents challenges such as the potential risk of cracking due to the intense energy input required [12]. On the other hand, any deformation in the SLM-printed samples can affect laser energy absorption during laser nitriding. A deformed surface can lead to the formation of an unstable melt pool, resulting in inconsistent surface properties in the nitride layer. The use of support structures can minimise post-detachment deformation after SLM, facilitating more uniform energy absorption during laser nitriding. It is believed that applying support structures to the samples before laser nitriding can enhance both the geometric integrity and surface properties of the nitrided Ti64 components.

The objectives of this research are as follows: 1) to implement support structures to minimise deformation during the SLM process and enhance the subsequent laser nitriding process, 2) to investigate how support structures influence the microstructure and porosity of the printed parts, 3) to apply laser nitriding post-SLM to enhance surface hardness, and 4) to create a crack-free nitride layer by manipulating the duty cycle between 50 % and 100 %.

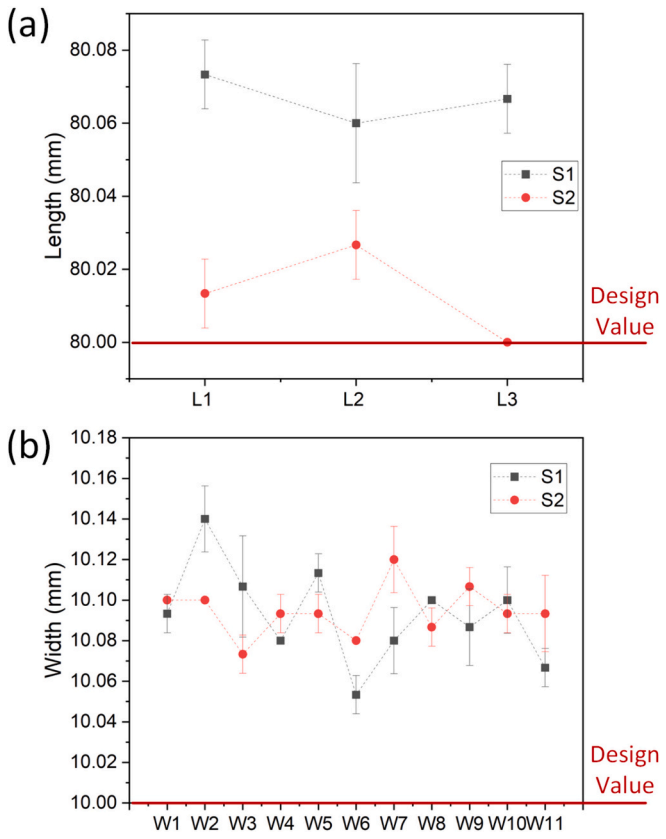

Fig. 5. (a) Length and (b) width measurements of as-printed samples: S1 and S2, obtained using vernier callipers before wire-cut separation from the substrate. Error bars represent $n = 3$ replicates. Data points without error bars indicate measurements with identical repeated results.

2. Methodology

2.1. Experimental workflow

The experimental workflow for this study is illustrated in Fig. 1. The samples were first prepared using SLM, after which their length and width were measured. Then, wire-cutting was performed to separate the samples from the substrate plate. The characterisation of the as-printed samples was then conducted, including analyses of deformation, porosity, phase composition, microstructure, and micro-hardness. Following this, the samples underwent post-processing via open-air laser nitriding. Characterisation analyses, such as surface colour and morphology, phase composition, microstructure, and micro-hardness, were also performed on the laser-nitrided samples. The details of each experiment are illustrated in the following sections.

2.2. Powder preparation

The Ti-6Al-4V (Ti64) powders used were sourced from SLM Solutions, Germany. The particle size and circularity were analysed by a morphological image analyzer (Malvern Morphologi 4, UK). The results were illustrated in Fig. 2 (a) and (b). The powders demonstrated a particle size distribution characterised by a d_{10} of 13.7 μm, d_{50} of 22.2 μm, and d_{90} of 40.8 μm. These powders exhibited high circularity with an average circularity of 0.95. Their morphology was further observed via a Scanning Electron Microscope (SEM, Tescan VEGA3, US), as illustrated in Fig. 2 (c). The chemical composition was analysed using an Energy Dispersive X-ray Spectroscope (EDX) equipped with the SEM, with results shown in Table 1. Before the SLM process, the powders were dried in a vacuum to a moisture content of around 7 %.

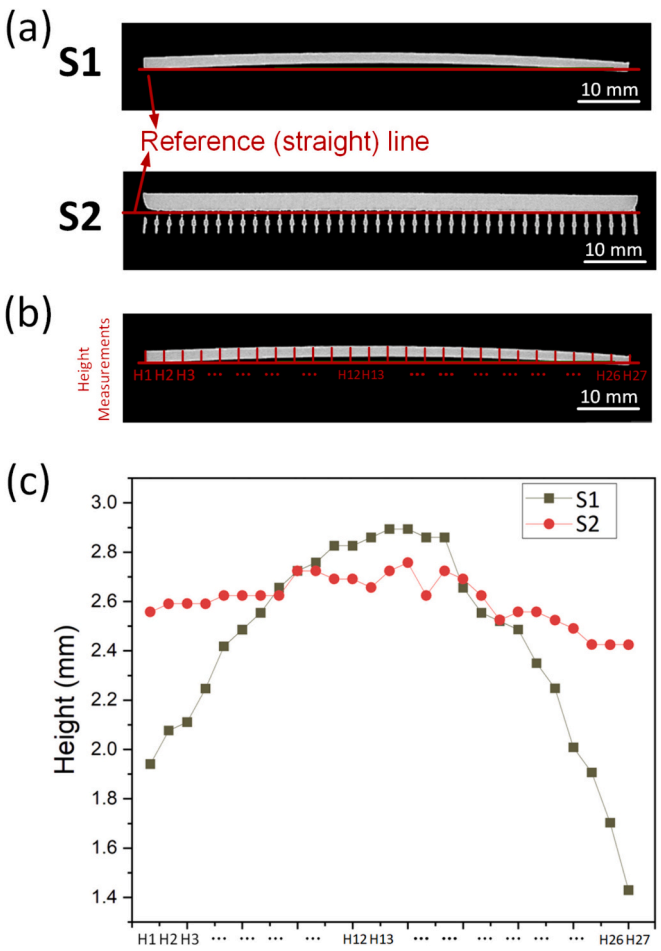

Fig. 6. (a) XCT overview of as-printed samples: S1 and S2 after separation from the substrate plate by wire-cutting. (b) Schematic diagram illustrating height measurements conducted using ImageJ. (c) Corresponding measurement results.

2.3. SLM fabrication process

A commercial SLM machine (SLM 280HL, SLM Solutions, Germany), equipped with a continuous wave (CW) Yb fiber laser operating at a wavelength of 1070 nm, was used for the SLM process. High aspect ratio Ti64 samples (80 mm × 10 mm × 2 mm), as depicted in the overview shown in Fig. 3 (a), were printed directly on the substrate plate (S1) or with support structure (S2). The printing was repeated three times to ensure repeatability. The single unit of support structure used in S2 is shown in Fig. 3 (b), with a height of 2.5 mm. It is repeated in two layers to support the sample, resulting in a total support height of 5 mm. The CAD model of S1 and S2 is presented in Fig. 3 (c).

The SLM process was conducted within an enclosed chamber filled with pure argon gas (99.999 %). The directional arrows in Fig. 3 (a) illustrate the gas flow from the inlet to the outlet. The use of argon is necessary for minimising oxidation and facilitating the removal of by-products, such as vapour plumes and spattering particles produced during SLM [13]. Throughout the entire process, the oxygen level was maintained below 0.2 %. Laser power of 275 W was applied with a scanning speed of 1100 mm/s, a hatch distance of 120 μm, and a layer thickness of 30 μm. These process parameters were carefully selected based on preliminary studies. The substrate plate, made of Ti-6Al-4V, was chosen to match the powder material, ensuring thermal and metallurgical compatibility between the substrate and the first layer of melted powder. Furthermore, the substrate plate was pre-heated to 200 °C before the printing process to mitigate residual stress.

2.4. Geometrical integrity and deformation analysis

To assess how the actual dimensions of the printed samples compared to their intended design values, the geometric dimensions, namely the length and width of samples S1 and S2, were measured. These measurements were taken while the samples remained fixed to the substrate plate. For each sample, the length was measured horizontally (from left to right), and the results were recorded as L1, L2, and L3. Additionally, the width of each sample was measured vertically (from front to rear), with the recorded dimensions being W1, W2… to W11. A schematic diagram illustrating these measurements is shown in Fig. 4. The measurements were carried out using vernier callipers, achieving an accuracy of up to 0.02 mm. To ensure the accuracy of these measurements, each dimension was measured three times.

Prior to further processing and detailed analysis, the as-printed samples were carefully detached from the substrate using wire-cutting technique. To evaluate the deformation the samples underwent after this procedure, X-ray Computed Tomography (XCT) was employed for an initial overview. Following XCT imaging, the ImageJ software was utilised to measure the height of the samples. The XCT analysis was conducted using the YXLON FF20 CT system from YXLON International GmbH, Germany. The settings for the XCT machine were as follows: a tube voltage of 190 kV and a tube current of 95 μA, with a total of 360 projections. Tin, with a 0.3 mm thickness, served as the filtering material to diminish noise in the XCT images.

2.5. XCT porosity analysis

The porosity levels of the as-printed samples were assessed using X-ray Computed Tomography (XCT) on the YXLON FF20 CT system. The samples were wire-cut to a smaller size to fit in the XCT machine. The size of samples S1 and S2 for porosity analysis is 12.5x10x2 mm^3. To ensure a uniform basis for comparison, the XCT parameters were standardised for all samples, with a tube voltage of 190 kV and a tube current of 100 μA. For each sample, a total of 1080 projections were acquired. Tin, with a thickness of 0.1 mm, served as the filter material. Following the XCT scans, porosity analysis was carried out using the Default algorithm within the VGStudio Max 3.0 software with a voxel size of 9.6 μm. It is noted that pores must occupy a minimum volume of 2 × 2 × 2 (8) voxels to be classified as a pore, aligning with the methodology of prior research [14,15].

2.6. Post-processing by open-air laser Nitriding

Laser nitriding was conducted on the as-printed samples in an open-air setup, shielded by N_2 gas. The nitriding process utilised a laser system from Micro Lasersystems BV, Driel, The Netherlands, equipped with a fiber laser produced by SPI Lasers, UK. The laser operated at a wavelength of 1064 nm. Following preliminary experiments, the laser power was established at 45 W, with a scanning speed of 25 mm/s. The distance between the laser nozzle and the samples, known as the stand-off distance, was maintained at 1.5 mm, resulting in a laser spot size of approximately 100 μm. Pure N_2 gas (99.99 %) was supplied coaxially with the laser beam, under a pressure of 6 bar, to protect the nitriding process from atmospheric contamination.

The duty cycle (DC), defined as the ratio of the laser active time (ON time) to the total cycle duration (ON + OFF time), was adjusted during the nitriding process to control the amount of energy delivered and to manage the cooling intervals between laser pulses. For example, a 50 % DC indicates the laser is active for half of the cycle. Preliminary nitriding experiments were conducted at DC settings of 50 % (DC50), 75 % (DC75), and 100 % (DC100). Each DC setting targeted a scanning area of 10 mm × 2 mm and was replicated three times to ensure result consistency. Table 2 lists the sample designations under different SLM and laser nitriding conditions. Post laser nitriding, the samples were cleaned with >99 % ethanol in an ultrasonic bath for 15 min to eliminate surface

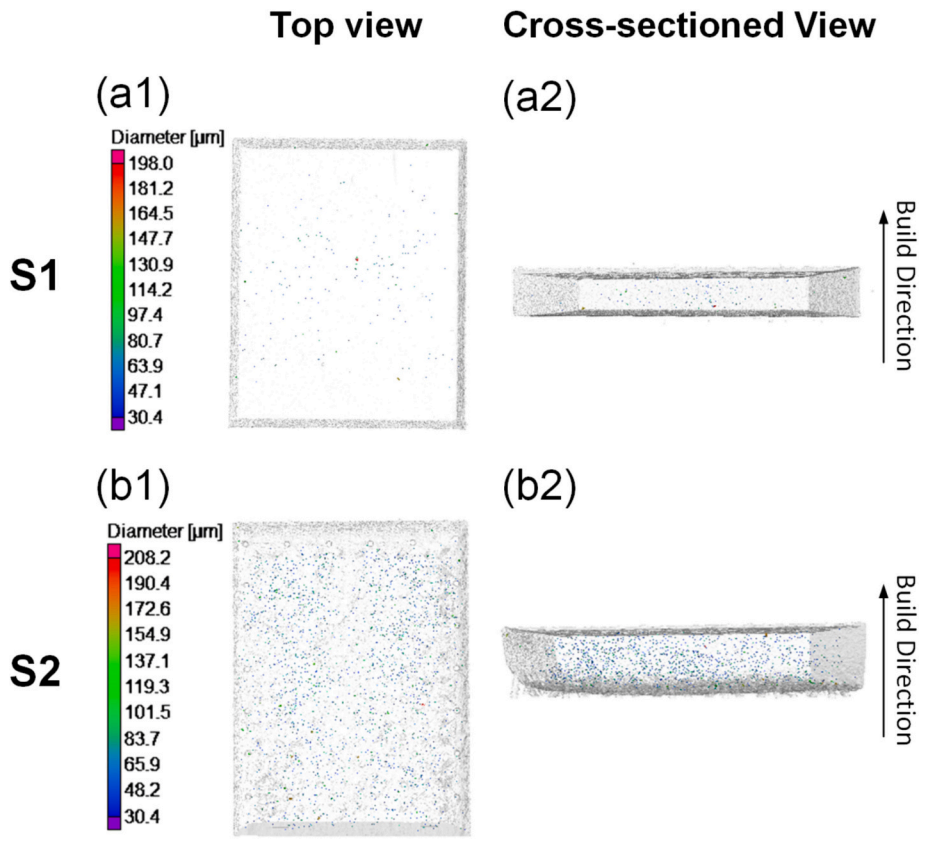

Fig. 7. XCT porosity analysis of as-printed samples: S1 and S2. (a1,b1) top view, (a2, b2) cross-sectioned view.

Table 3
Porosity characteristics of S1 and S2 samples by XCT.

Sample	S1	S2
Pore Volume Fraction (%)	0.003 %	0.03 %
Number of Pores	349	5677
Minimum Pore Diameter (μm)	30.4	30.4
Maximum Pore Diameter (μm)	198	208.2
Average Pore Diameter (μm)	52.4 ± 20.0	53.8 ± 17.4

contaminants, followed by air drying to ensure thorough cleanliness.

2.7. Surface colour and morphology analysis

The surface colour of the laser-nitrided samples was examined using an optical microscope that included a digital camera (AmScope MU2003, United Scope Europe BV, Netherlands) and a monocular microscope (AmScope H800-3PL, United Scope Europe BV, Netherlands). For a closer analysis of the top surface morphology, a Scanning Electron Microscope (SEM, Hitachi TM3000, Japan) was used.

2.8. Characterisation analysis of As-printed and laser-nitrided samples

2.8.1. XRD phase analysis

X-ray Diffraction (XRD) analysis was performed on both the as-printed and laser-nitrided samples to examine their phase structures, utilising a Rigaku SmartLab X-ray Diffractometer (Japan). The analysis employed Cu Kα radiation (λ = 1.5406 Å), with the operational settings of 45 kV for voltage and 200 mA for current. The scanning was conducted at a speed of 2°/min, spanning a diffraction angle range (2θ) from 20° to 60°. Phase identification within the samples was based on diffraction angle data sourced from ICDD 00–001-1198, ICDD 01–073-1583, ICDD 01–087-0632, complemented by findings from the study by Artur [16].

2.8.2. Microstructural characterisation by SEM

The cross-sectional microstructures of the as-received and laser-nitrided samples were examined using a field emission SEM (Tescan MIRA, US). For SEM imaging preparation, the samples followed a standard procedure starting with cutting, then embedding in epoxy resin. The samples were subsequently polished through a graded series of sandpapers with grits P240, P320, P400, P800, P1200, P2000, and P3000. After the polishing process, the samples were ultrasonically cleaned in ethanol for 10 min to remove any residual polishing debris. The final step in sample preparation involved etching with Kroll's reagent (a mixture of 1 % HF solution, 5 % HNO3 solution, and 94 % distilled water) for approximately 1 min, to enhance the visibility of the microstructure.

2.9. Micro-hardness analysis

Vickers micro-hardness testing was conducted on the laser-nitrided zone (LNZ) and base metal (BM) of nitrided samples using a Struers Duramin-40 machine (Denmark). A force of 200 gf and a dwell time of 20 s were employed during testing. Indentations were carefully placed starting from the LNZ on the surface and extending to the BM beneath. The testing protocol included one indentation in the LNZ and seven in the BM for each sample, maintaining a 50 μm gap between indentations. To ensure the reliability of the results, the hardness test was replicated four times for the laser-nitrided samples, resulting in a total of 32 indentations, i.e., 4 in the LNZ ($n = 4$) and 28 in the BM ($n = 28$). The terms S1BM and S2BM represent the BM of the S1 and S2 samples after nitriding, respectively, whereas S1DC50 and S2DC50 designate the LNZ within those same sample.

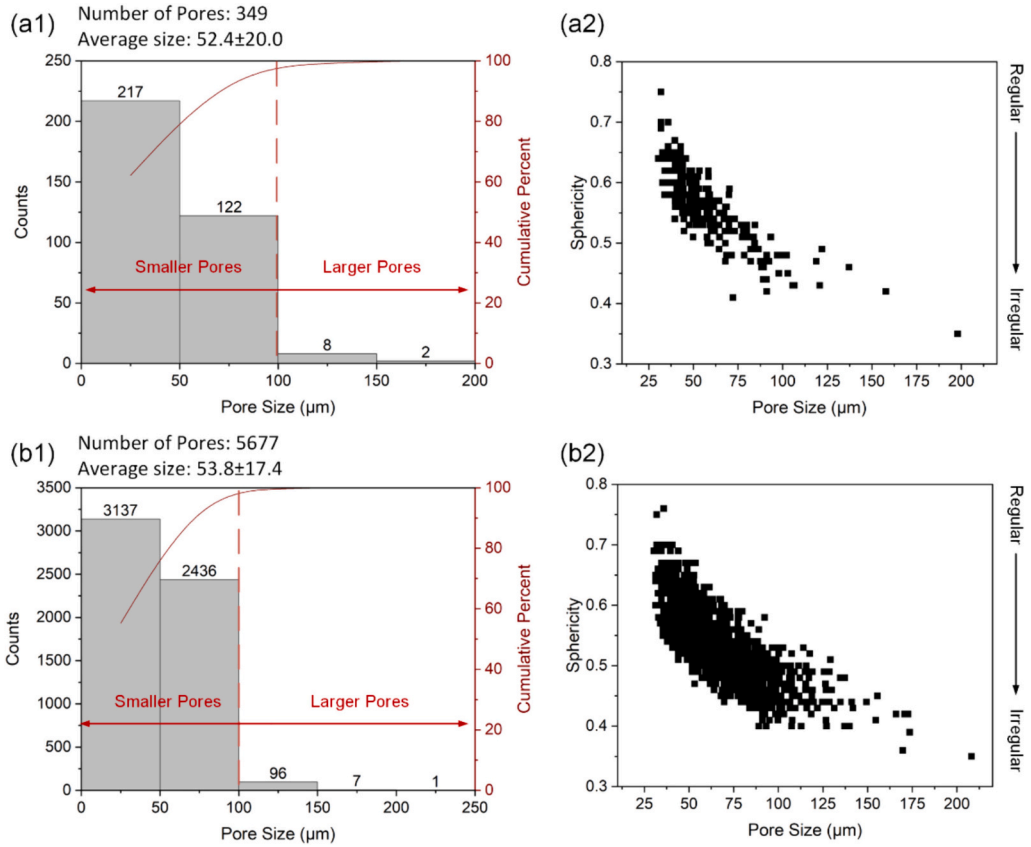

Fig. 8. Pore statistics obtained from S1 (a1, a2) and S2 (b1, b2): pore size distribution (a1, b1) and scatter plot of pore sphericity as a function of pore size (a2, b2).

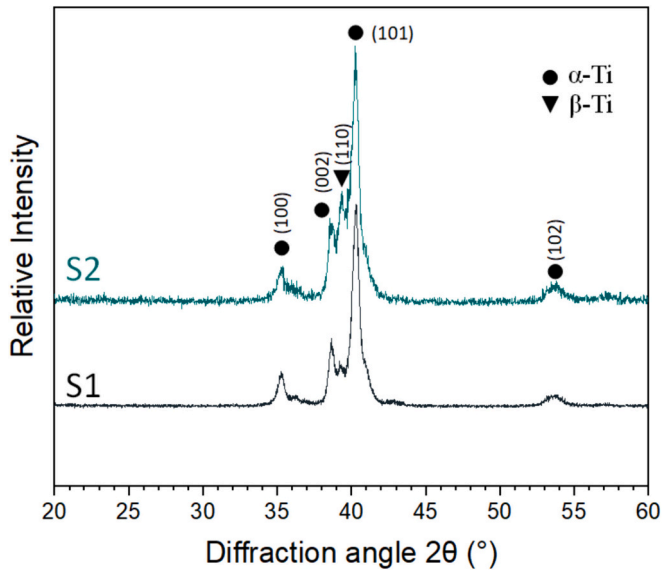

Fig. 9. XRD phase analysis of as-printed samples: S1 and S2, presenting phase angles from 20° to 60°.

3. Results and discussion

3.1. As-printed samples by SLM

3.1.1. Geometrical integrity & deformation analysis of as-printed samples

The deformation analysis results, shown in Fig. 5, reveal slight discrepancies in the dimensions of S1 and S2 samples compared to their design values. As shown in Fig. 5(a), both S1 and S2 exhibit lengths marginally exceeding the intended design, with S1 showing a deviation of <0.1 % and S2 <0.04 %, indicating the length of S2 approaches more closely the design value than that of S1. In terms of width, as depicted in Fig. 5(b), both samples also exceed the design values, with S1 having a variance of <1.4 % and S2 <1.2 %. The width of S1 shows higher variability across measurements compared to S2. These dimensional variances are attributed to the thermal history of SLM which involves rapid heating and cooling of the Ti64 material, leading to thermal expansion and contraction that affect the final dimensions.

Post wire-cut separation, the XCT imaging in Fig. 6(a) reveals notable warping in S1, while S2 appears more uniform in shape. Quantitative deformation analysis, as presented in Fig. 6(b) and summarised in Fig. 6(c), shows that the height of S1 increases from approximately 1.9 mm to 2.9 mm at the midpoint, then decreasing to about 1.4 mm at the other end. Conversely, S2 exhibits a more stable height variation between 2.4 mm and 2.7 mm. The significant thermal gradients generated during SLM result in uneven cooling rates and residual stresses, which can cause deformations once the part is removed from the substrate, especially in the samples with high aspect ratios that are prone to bending and distortion. The thermal effects of the wire-cutting process can further aggravate these stresses, leading to increased deformation.

The small distortion in S2 can be attributed to the presence of a support structure. As depicted in Fig. 3(c), the support structure is designed to minimise the contact area between the sample and the substrate, achieved through strategic placement and geometry. This support enhances heat dissipation during SLM, thus reducing the accumulation of residual stresses. Additionally, thermal impact during wire-cutting is also reduced, thereby preserving the integrity and precision of the printed part post wire-cutting.

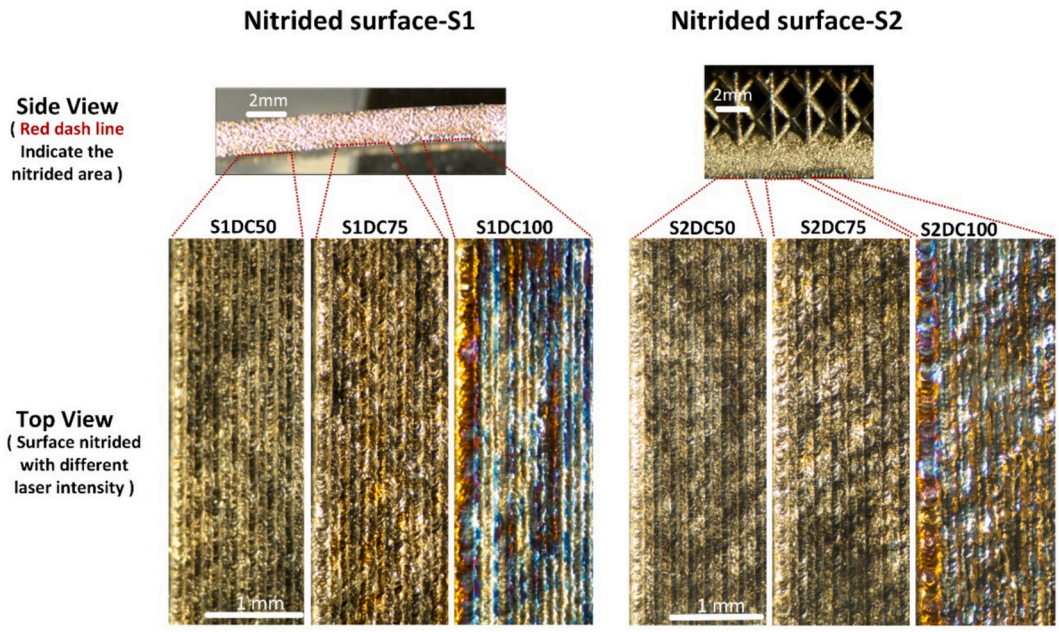

Fig. 10. Top surface morphology and colour of S1 and S2 following laser nitriding process, as observed through an optical microscope.

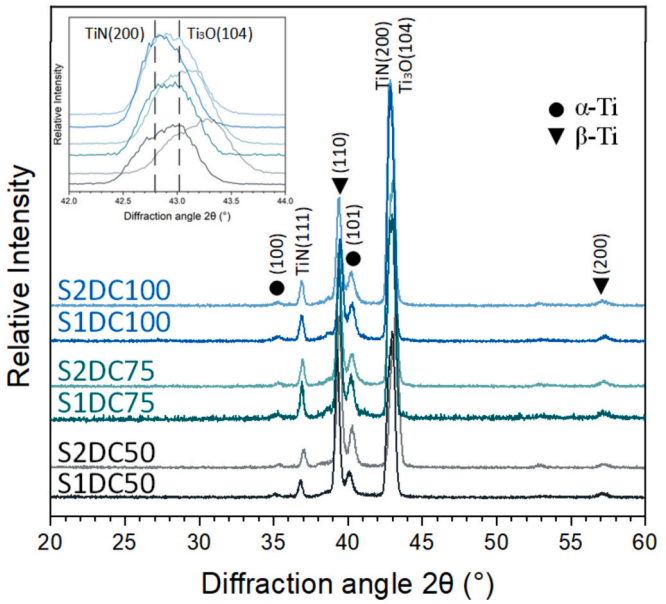

Fig. 11. XRD phase analysis of all nitrided samples, presenting phase angles from 20° to 60°. An enlarged view of the region from 42° to 44° is displayed in the upper left corner.

3.1.2. XCT porosity analysis of As-printed samples

Fig. 7 presents the XCT porosity analysis for samples S1 and S2. Table 3 summarizes these findings, listing porosity characteristics. In addition, Fig. 8 summarizes the pore statistics obtained from Fig. 7, including pore size distribution and scatter plot of pore sphericity as a function of pore size.

There are 349 pores identified in S1, with diameters ranging from 30.4 μm to 198 μm, and an average diameter of 52.4 ± 20.0 μm. The porosity volume fraction in S1 is 0.003 %. In contrast, the S2 sample demonstrated higher porosity levels, with 5677 pores occupying a volume fraction of 0.03 %. The pore diameters in S2 ranged from 30.4 μm to 208.2 μm, with an average size of 53.8 ± 17.4 μm.

Pores were classified into two groups based on size: smaller (<100 μm) and larger (≥100 μm). As shown in Fig. 8 (a1) and (b1), although S2 has a higher number of both smaller and larger pores, >97 % of the pores in both samples are in the smaller category. Pore sphericity, which varies from 0 to 1 (with values closer to 1 indicating a more spherical shape), was used to assess pore shape. As illustrated in Fig. 8 (a2) and (b2), the pore sphericity in both samples ranges from 0.3 to 0.8. Moreover, larger pores tend to have lower sphericity, indicating that they are less spherical in shape.

The comparison between S1 and S2 reveals that S1, which was printed directly onto the substrate, exhibited lower porosity volume fractions, suggesting a more effective melting and solidification process. This is due to the uninterrupted contact between the powder and the substrate, facilitating better energy absorption and powder melting. On the contrary, the increased porosity of S2 is attributed to the introduction of support structures, which may disrupt direct powder bonding.

3.1.3. XRD phase analysis of As-printed samples

The phase composition of samples S1 and S2, as determined by XRD within the diffraction angle range of 20° to 60°, is illustrated in Fig. 9. This analysis demonstrates that the peak positions for both S1 and S2 align identically, indicating the coexistence of both α-Ti and β-Ti phases in each sample.

The dominant α peaks are observed from the (101) planes at 40.42°, alongside the less pronounced α peaks at 35.31° (100), 38.44° (002), and 53.21° (102). These planes can influence the crystal orientation of the Ti64 materials, thereby affecting their mechanical characteristics and phase stability [17]. Furthermore, the β phase peaks, identifiable at 39.20° from the (110) planes, exhibit higher intensity in S2 compared to S1. This indicates a higher concentration of the β-Ti phase in S2 within the examined region. Such disparity is linked to the support structure in S2, which modifies the thermal history of the components during the SLM process, potentially influencing phase formation and its stability.

3.2. Post-processing by open-air laser nitriding

3.2.1. Surface colour analysis of nitrided samples

The surface morphology and colour variations in samples S1 and S2, subjected to laser nitriding at different duty cycles, are illustrated in Fig. 10. This process involves the reaction of titanium with nitrogen to form titanium nitride (TiN), a compound whose colour shifts depending

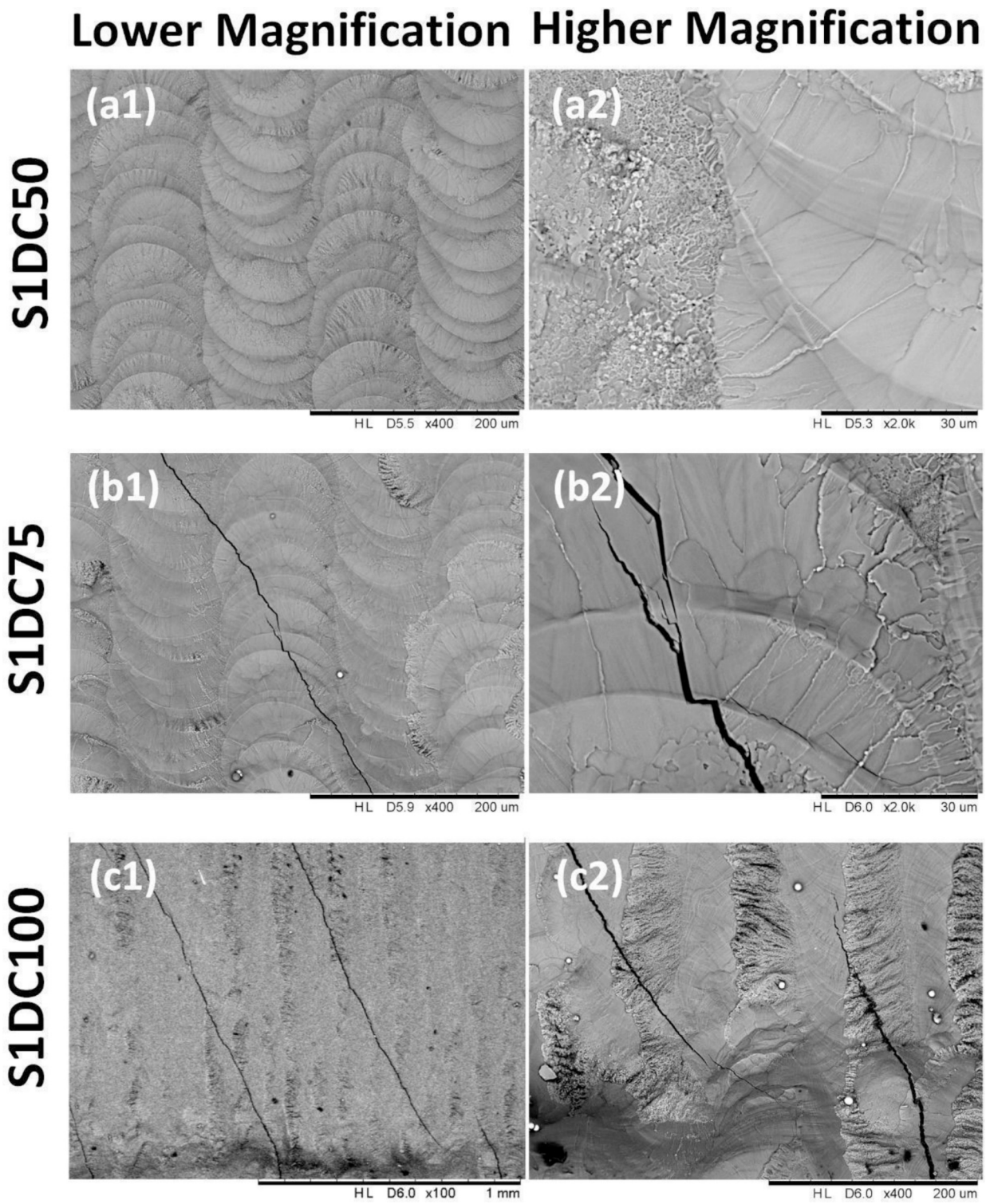

Fig. 12. Top surface morphology of S1DC50, S1DC75 and S1DC100. (a1-c1) SEM micrographs at lower magnification of x100; (a2-c2) at higher magnification of x400.

on the nitrogen concentration absorbed by the surface [12].

At a 50 % duty cycle, both nitrided samples (denoted as S1DC50 and S2DC50), display predominantly dark brown hues interspersed with lighter regions. Increasing the duty cycle to 75 % results in S2DC75 retaining a similar colour scheme but with fewer dark areas, while S1DC75 transitions to a blend of golden, dark brown, and lighter patches. Further increasing the duty cycle to 100 % induces notable discolouration in both S1DC100 and S2DC100 samples. This change is attributed to oxygen intrusion from the surrounding air during the nitriding process, leading to the formation of surface oxides like TiO_2 and TiNxOy, as explained in [18]. The diversity in oxide colours correlates directly with the oxide film thickness [19].

This analysis indicates that increased duty cycles can lead to a higher variation in oxide layer thickness, as evidenced by the surface colour differences of the nitrided samples. Additionally, the oxide layer on S1 appears to have less uniform thickness than that on S2. Such variation

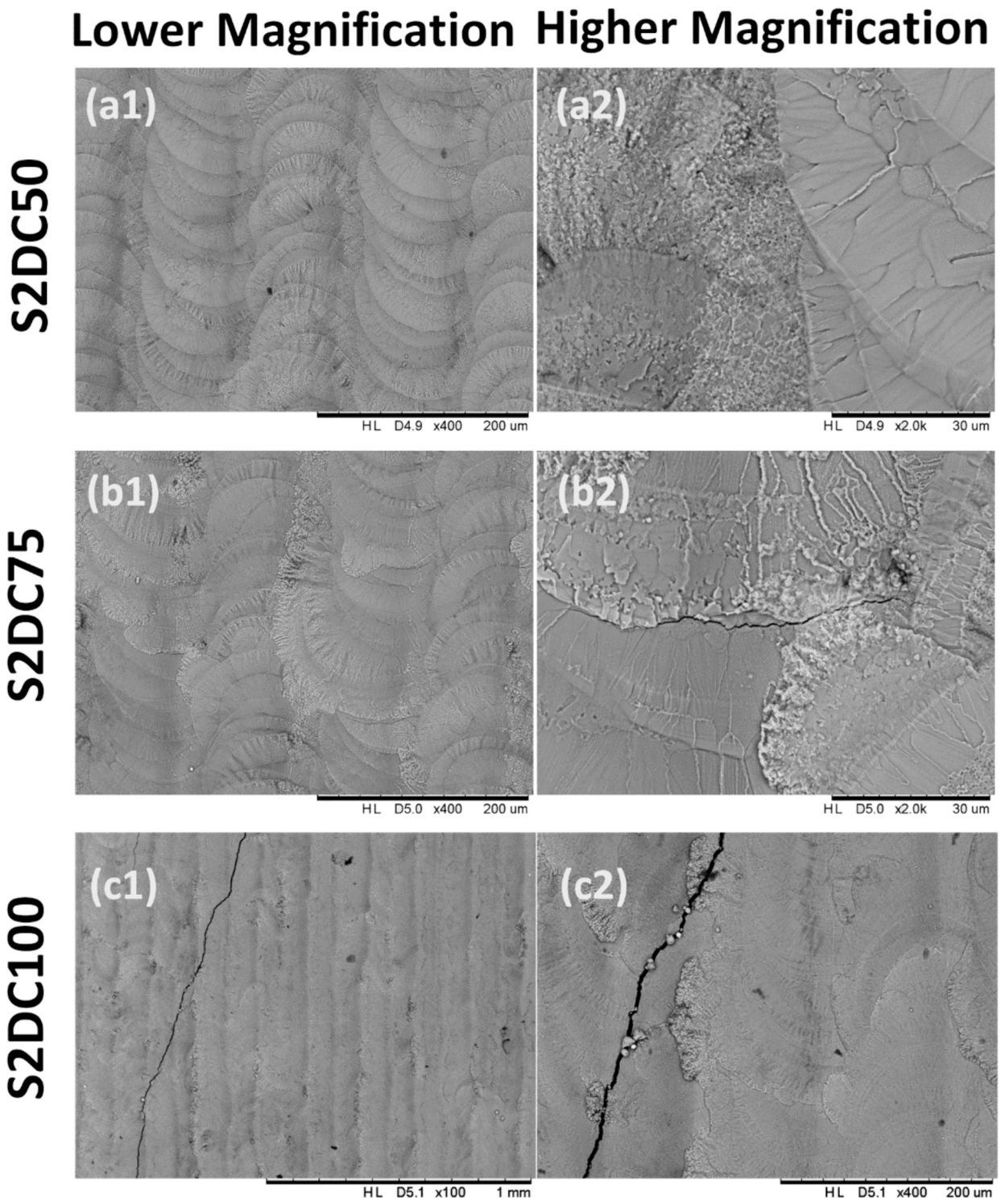

Fig. 13. Top surface morphology of S2DC50, S2DC75 and S2DC100. (a1-c1) SEM micrographs at lower magnification of x100; (a2-c2) at higher magnification of x400.

can be attributed to the bent surface of S1, as seen in Fig. 6(a), which leads to fluctuations in the stand-off distance and consequently the laser spot size during the nitriding process. These fluctuations cause uneven laser intensity across various sections, ultimately resulting in a more heterogeneous oxide layer.

3.2.2. *XRD phase analysis of Nitrided samples*

Fig. 11 displays the XRD results of samples S1 and S2 after laser nitriding, spanning a diffraction angle range from 20° to 60°. The peak positions are consistent across all nitrided samples. Two main peaks at around 42.77° and 43.01° indicate the formation of TiN (200) and Ti_3O (104), respectively. Upon a closer examination of the diffraction curves from 42° to 44°, as shown in the upper left corner of Fig. 11, peak shifts are observed in S2. This implies subtle changes in crystal lattice, resulting from different thermal history and stress distribution due to the support structure used in S2. The TiN phase is further evidenced by peaks at 36.82°, associated with the (111) planes. Additionally, α phase peaks are identified at 35.31° (100) and 40.42° (101), and β phase peaks

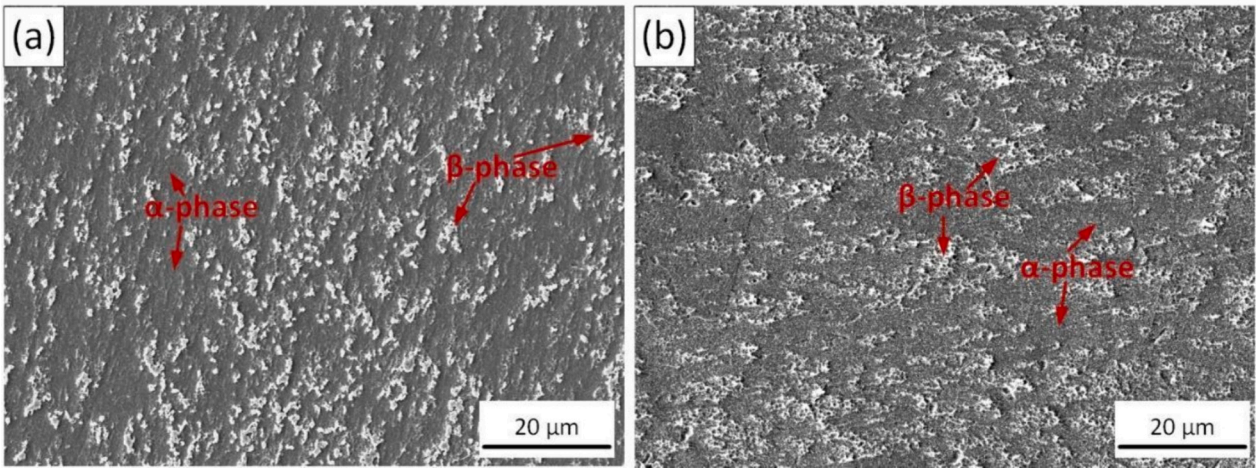

Fig. 14. Cross-sectional SEM micrograph of BM microstructure in as-printed samples: (a) S1 and (b) S2.

are seen at 39.20° (110) and 57.40° (200).

Compared to the as-printed samples, a significant change in the phase structure is observed, with the emergence of titanium nitride (TiN) and titanium oxide (Ti_3O). It is important to note that other titanium nitride phases, such as Ti_2N and Ti_3N_4, exist in addition to TiN. TiN is a compound well-known for its high elastic modulus and hardness [20]. The detection of the TiN phase in this study aligns with the findings of Chan et al. [12], who observed similar phenomena in laser-nitrided TiNb alloys. Furthermore, the α peaks at 40.42° (101), which were the most prominent in the as-printed samples, appear weaker than the β peaks at 39.20° (110) in the nitrided samples. This suggests a phase transition from α to β phase, triggered by the thermal effects of laser nitriding. The impact of the support structure in S2 on the phase structure post-laser nitriding is minimal, as shown by the insignificant differences in peak positions between the nitrided S1 and S2.

3.2.3. *Surface morphology analysis of Nitrided samples*

Surface morphology analysis is important for evaluating the success of laser-nitrided surfaces, aimed at achieving complete nitride coverage without cracks. Given the high hardness of TiN, regions that are not nitrided remain comparatively less protected and are therefore more susceptible to mechanical or corrosion failures. To ensure comprehensive nitride coverage, proper overlapping between laser tracks is essential. Cracks can form if the thermal stress build-up during the process exceeds the tensile strength of the samples within the melt pool, aggravated by the limited plastic deformation capacity of TiN under stress [21].

The surface morphology of samples S1 and S2 after laser nitriding, captured by SEM, is shown in Figs. 12 and 13, respectively. The laser tracks fully cover the surface, regardless of the duty cycle used. At a 50 % duty cycle, S1DC50 and S2DC50 exhibit densely populated laser tracks with ripple structures (Fig. 12 (a1) and 13 (a1)), with no visible cracks (Fig. 12 (a2) and 13 (a2)). At a 75 % duty cycle, S1DC75 exhibits a prominent crack aligned with the laser scan direction (Fig. 12 (b1)), alongside branching microcracks originating from the primary crack (Fig. 12 (b2)). On the contrary, S2DC75 lacks larger cracks but shows micro-cracks (Fig. 13 (b1, b2)), attributed to the support structure in S2 that helps mitigate thermal stress accumulation and thus reduce crack formation. Increasing the duty cycle to 100 % exacerbates the length and number of cracks (Fig. 12 (c1, c2) and 13 (c1, c2)), as higher energy input from the laser enhances thermal stress and facilitates crack growth. These cracks can significantly undermine the mechanical and corrosion resistance of the samples, acting as stress concentration points and pathways for corrosive fluids.

Given these observations, the nitrided samples chosen for detailed microstructure characterisation in Section 3.3 and for micro-hardness analysis in Section 3.4 were those processed at a 50 % duty cycle. The selection criterion was based on their crack-free surfaces and the uniform golden hue they exhibited, which are indicative of successful laser nitriding and optimal condition for further evaluation.

3.3. *Microstructural characterisation by SEM*

3.3.1. *Microstructure in as-printed samples*

The cross-sectional SEM micrographs presented in Fig. 14 contain distinct light and dark regions, indicating a multiphase microstructure in both S1 and S2 samples. The dark regions correspond to the α-phase of Ti64, while the bright areas indicate the presence of β-phase. The key contrast between S1 and S2 microstructure in the as-built condition is the clustering density of the β-phase, with S1 exhibiting a higher clustering density of β-phase than S2. The residual stress incurred during the printing process influences phase transformation kinetics and distribution [22]. The support structure in S2 can aid in residual stress mitigation and distribute the β-phase more evenly, providing a more uniform microstructure.

3.3.2. *Microstructure in nitrided samples*

The microstructures of the nitrided samples, S1DC50 and S2DC50, are illustrated in Fig. 15. Two perceptible zones exist in both samples: the LNZ at the surface, indicated by dendritic structures and an irregular melt pool boundary, and the BM below the LNZ, which retains its original microstructural characteristics. The reaction between Titanium and Nitrogen during the formation of TiN dendrites during the laser nitriding process is exothermic. The additional heat input from this reaction causes localised melting and contributes to the formation of an irregular boundary around the nitride layer. The formation of a mushy zone may also play a role in the irregularity of the boundary due to the arresting mechanism of dendrite formation on the solidification front. Despite the irregular boundary, and differing initial microstructures in the BM, the mean depth of the LNZ, measured from ten different locations, was nearly identical for S1DC50 and S2DC50, 36.3 μm and 36.0 μm, respectively. In S1DC50, the presence of an irregularly shaped island of BM within the LNZ was detected. There are several potential explanations, including short-term laser malfunction, however further study would be required to determine the exact formation mechanism. Regardless, the lack of TiN dendrites may have a detrimental impact on the local material properties, particularly hardness.

Detailed microstructural views at the top of the LNZ of both S1DC50 and S2DC50 (Fig. 15 (b1) and (b2)) show short dendritic formations with varied orientations. However, S2DC50 exhibits a higher density of TiN dendrites which exhibit a finer structure than those in S1DC50. Beyond the region of short, randomly orientated dendrites, the dendrites

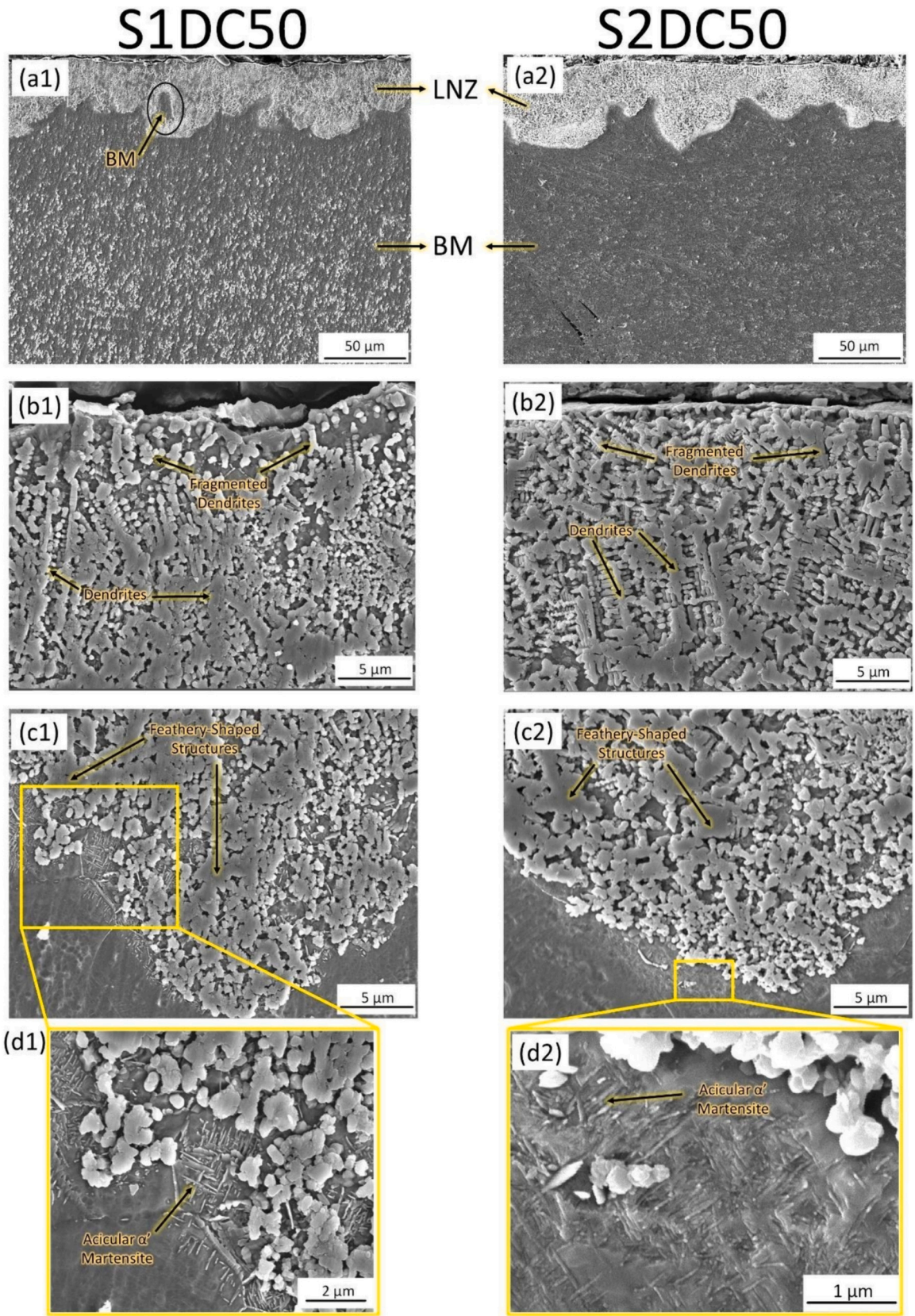

Fig. 15. SEM images showcasing the microstructures of nitrided samples: S1DC50 and S2DC50. (a1) and (b2) provide an overview of the LNZ for S1DC50 and S2DC50, respectively; (b1) and (b2) detail the top of the LNZ; (c1) and (c2) show the lower regions of the LNZ; and (d1) and (d2) magnify the fine needle-like structures beneath the nitride layer.

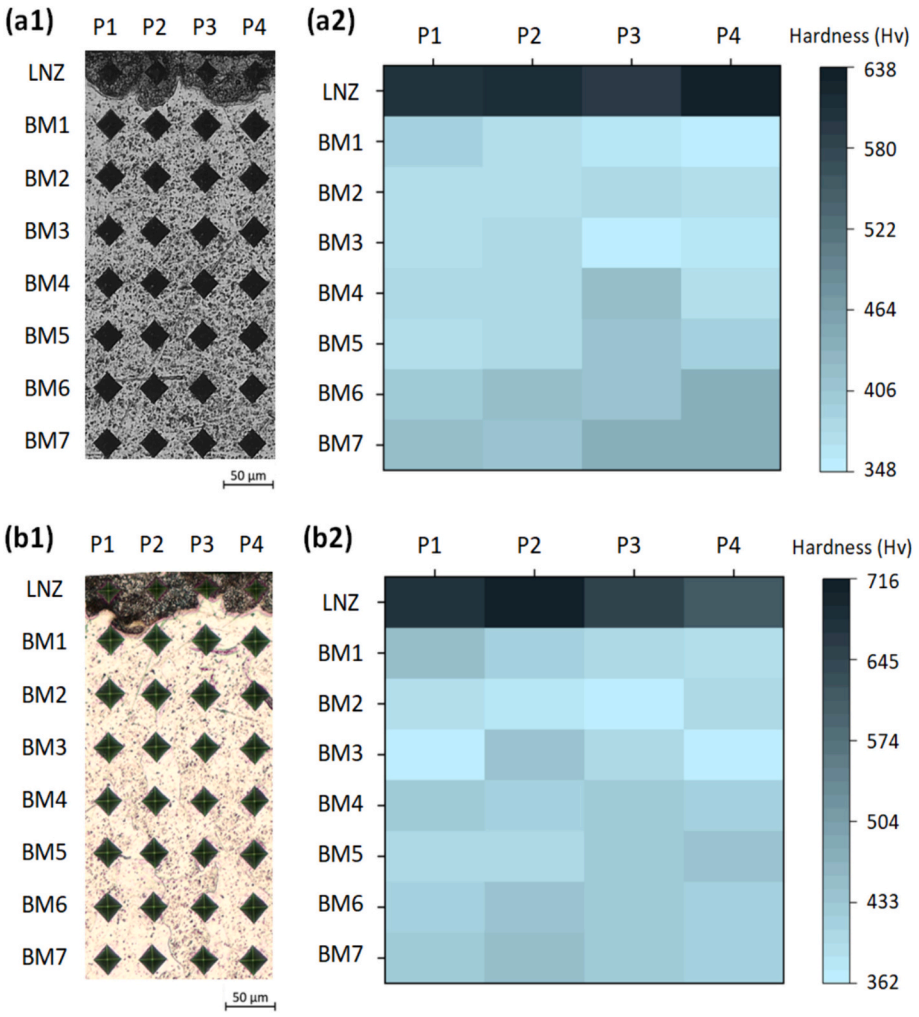

Fig. 16. Micro-hardness distribution and indentation analysis: (a1) and (b1) show optical images of indentation marks on the LNZ and BM for the samples S1 and S2 after laser nitriding, respectively. (a2) and (b2) present 2D hardness maps based on measurements from the nitrided samples, with P1 to P4 denoting distinct positions across the samples for comparative analysis.

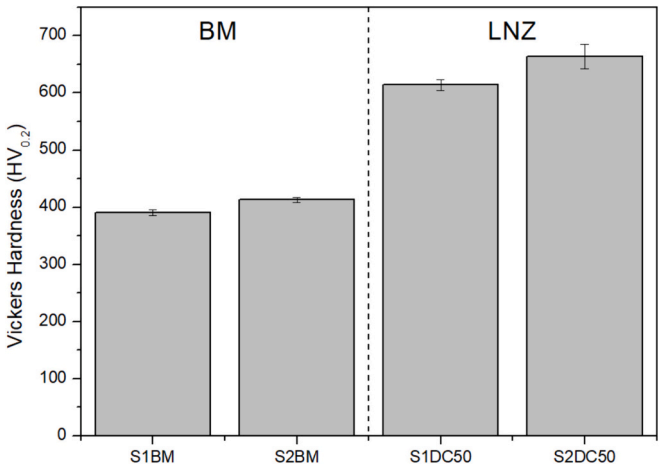

Fig. 17. Bar chart showing the comparative Vickers hardness (HV0.2) of laser-nitrided samples. S1BM and S2BM indicate the BM hardness, respectively, while S1DC50 and S2DC50 represent the hardness of the LNZ. Error bars signify the standard error (SE) of $n = 28$ for S1BM and S2BM; $n = 4$ for S1DC50 and S2DC50.

lengthen and orientate near-perpendicular to the surface. In S1DC50, the density of dendritic structures increases, although still not to the same level demonstrated by S2DC50.

Lower regions of the LNZ (Fig. 15 (c1) and (c2)) reveal fewer and more fragmented dendrites due to non-uniform solidification influenced by forced convection within the melt pool. The transition to a feathery-dominated microstructure is obvious in both samples, although less prevalent than in S1DC50. The feathery structures occur as the flow develops into a mushy zone, due to stagnation effects, which occur as advancing dendrites increase melt pool viscosity and obstruct molten flow, as well as localised areas of high nitrogen concentration within the microstructure.

Directly beyond the nitride layer (Fig. 15 (d1) and (d2)), fine needle-shaped structures indicate a heat-induced martensitic transformation as acicular α' martensite develops. This martensitic phase, formed from rapid cooling that suppresses α-phase formation, was not detected by XRD due to its depth beyond the X-ray penetration limit in titanium, typically around 10 µm [23]. The potential for acicular martensite to improve the material properties, specifically hardness, has been demonstrated previously [24].

3.4. Micro-hardness analysis

Fig. 16 provides a comparative analysis of the micro-hardness distribution across the BM and LNZ of the samples S1 and S2 after laser

nitriding. The nitrided samples selected for hardness testing were in optimal condition at a 50 % duty cycle, with their crack-free surfaces and uniform golden colour indicating successful laser nitriding. The 2D hardness maps (see Fig. 16 (a2) and (b2)) reveal a significant increase in hardness within the LNZ compared to the BM for both samples. This increase is due to the formation of TiN within the LNZ from the laser nitriding process. Fig. 17 presents a bar chart comparing the average hardness values of the BM and LNZ for the nitrided samples. The bar chart indicates a significant increase from 390.1 ± 4.92 HV0.2 for S1BM to 613.8 ± 9.45 HV0.2 for S1DC50. Similarly, there is an increase from 412.7 ± 4.31 HV0.2 for S2BM to 663.8 ± 21.12 HV0.2 for S2DC50. Both S2BM and S2DC50 exhibit a higher average hardness compared to S1BM and S1DC50, respectively. The increase in hardness for S2BM can be attributed to its more refined microstructure, as evidenced by SEM micrographs (refer to Fig. 14 (b)). Interestingly, despite the higher porosity levels observed in S2, there is no corresponding reduction in hardness. In addition, the enhanced hardness in S2DC50 is a result of the formation of finer dendritic structures, as shown in Fig. 15 (b2) and (c2).

4. Conclusions

In this study, high aspect ratio Ti-6Al-4V samples were fabricated using SLM technique, with the use of support structures (S2) and without the use of support structures (S1). After wire-cutting the samples from the substrate, deformation and porosity analysis were performed to assess the effects of support structures. Subsequently, these samples underwent laser nitriding with modulated duty cycles (50 %–100 %) to create crack-free, hard nitride layers. The major findings are outlined as follows:

- Both S1 and S2 exhibited dimensions slightly larger than their design specifications, though S2 was closer to the intended dimensions. After the samples were detached from the substrate using wire-cutting, warping was observed in S1, whereas S2 exhibited minimal deformation. This indicates that support structures effectively ensure geometrical integrity and reduce thermal-induced deformation.
- While S2 exhibited an increase in porosity, it also demonstrated a more refined microstructure, contributing to increased hardness.
- Laser nitriding at a 50 % duty cycle resulted in uniform, crack-free TiN layers on both S1 and S2, significantly enhancing their surface hardness.
- The application of support structures did not alter the phase structure of the nitrided layer, but it facilitated the formation of finer TiN dendrites within the nitride layers. These finer dendrites contributed to a further enhancement of the surface hardness of S2 after laser nitriding.

CRediT authorship contribution statement

Weijie Xie: Writing – original draft, Investigation, Formal analysis, Data curation. **Conall Kirk:** Writing – original draft, Investigation. **Amal Rejee:** Writing – original draft, Investigation. **Hau-Chung Man:** Writing – review & editing, Supervision, Funding acquisition. **Chi-Wai Chan:** Writing – review & editing, Supervision, Methodology, Funding acquisition, Conceptualization.

Declaration of competing interest

The authors declare that they have no known competing financial interests or personal relationships that could have appeared to influence the work reported in this paper.

Data availability

Data will be made available on request.

Acknowledgements

The work described in this paper was fully supported by a grant from the Research Grants Council of the Hong Kong Special Administrative Region (152131/18E). Support from the infrastructure of The Queen's University Belfast, The Hong Kong Polytechnic University and University Research Facility in 3D Printing(U3DP) is also acknowledged.

References

[1] R. Nandhakumar, K. Venkatesan, A process parameters review on selective laser melting-based additive manufacturing of single and multi-material: microstructure, physical properties, tribological, and surface roughness, Materials Today Communications 35 (2023) 105538.
[2] A.K. Singla, et al., Selective laser melting of Ti6Al4V alloy: process parameters, defects and post-treatments, J. Manuf. Process. 64 (2021) 161–187.
[3] Q. Jiang, et al., A review on additive manufacturing of pure copper, Coatings 11 (2021), https://doi.org/10.3390/coatings11060740.
[4] D. Thomas, R. Bibb, Identifying the geometric constraints and process specific challenges of selective laser melting, in: Proceedings of Time Compression Technologies Rapid Manufacturing Conference, Coventry, United Kingdom, 2008.
[5] M.X. Gan, C.H. Wong, Practical support structures for selective laser melting, J. Mater. Process. Technol. 238 (2016) 474–484.
[6] J. Xiaohui, et al., Effect of supporting structure design on residual stresses in selective laser melting of AlSi10Mg, Int. J. Adv. Manuf. Technol. 118 (5) (2022) 1597–1608.
[7] T. Kurzynowski, et al., Effect of scanning and support strategies on relative density of SLM-ed H13 steel in relation to specimen size, Materials (Basel) 12 (2) (2019).
[8] D. Palmeri, et al., Sample building orientation effect on porosity and mechanical properties in selective laser melting of Ti6Al4V titanium alloy, Mater. Sci. Eng. A 830 (2022) 142306.
[9] Y. Cui, et al., Effect of porosity on dynamic response of additive manufacturing Ti-6Al-4V alloys, Micromachines 13 (2022), https://doi.org/10.3390/mi13030408.
[10] J. Stef, et al., Mechanism of porosity formation and influence on mechanical properties in selective laser melting of Ti-6Al-4V parts, Mater. Des. 156 (2018) 480–493.
[11] P. Kumar, O. Prakash, U. Ramamurty, Micro-and meso-structures and their influence on mechanical properties of selectively laser melted Ti-6Al-4V, Acta Mater. 154 (2018) 246–260.
[12] C.-W. Chan, et al., A single parameter approach to enhance the microstructural and mechanical properties of beta Ti-Nb alloy via open-air fiber laser nitriding, Surf. Coat. Technol. 383 (2020) 125269.
[13] G.E. Bean, et al., Process gas influence on microstructure and mechanical behavior of Inconel 718 fabricated via selective laser melting, Progress in Additive Manufacturing 5 (4) (2020) 405–417.
[14] S. Tammas-Williams, et al., XCT analysis of the influence of melt strategies on defect population in Ti–6Al–4V components manufactured by selective electron beam melting, Mater Charact 102 (2015) 47–61.
[15] W. Xie, H.-C. Man, C.-W. Chan, Interplay of laser power and pore characteristics in selective laser melting of ZK60 magnesium alloys: a study based on in-situ monitoring and image analysis, Journal of Magnesium and Alloys 15 (2023) 1346–1366.
[16] A.R. Shugurov, et al., Recovery of scratch grooves in Ti-6Al-4V alloy caused by reversible phase transformations, Metals 10 (2020), https://doi.org/10.3390/met10101332.
[17] Y. Qi, et al., Effect of crystallographic orientation on mechanical properties of single-crystal CoCrFeMnNi high-entropy alloy, Mater. Sci. Eng. A 814 (2021) 141196.
[18] C.-W. Chan, et al., Fibre laser nitriding of titanium and its alloy in open atmosphere for orthopaedic implant applications: investigations on surface quality, microstructure and tribological properties, Surf. Coat. Technol. 309 (2017) 628–640.
[19] M.V. Diamanti, B. Del Curto, M. Pedeferri, Interference colors of thin oxide layers on titanium, Color Research & Application 33 (3) (2008) 221–228.
[20] S. Yu, et al., Phase stability, chemical bonding and mechanical properties of titanium nitrides: a first-principles study, Phys. Chem. Chem. Phys. 17 (2014).
[21] M. Li, K. Huang, X. Yi, Crack formation mechanisms and control methods of laser cladding coatings: a review, Coatings 13 (2023), https://doi.org/10.3390/coatings13061117.
[22] A. Mertens, et al., Microstructure and properties of SLM AlSi10Mg: understanding the influence of the local thermal history, Procedia Manufacturing 47 (2020) 1089–1095.
[23] S. Malinov, et al., Synchrotron X-ray diffraction study of the phase transformations in titanium alloys, Mater Charact 48 (4) (2002) 279–295.
[24] J. He, et al., The martensitic transformation and mechanical properties of Ti6Al4V prepared via selective laser melting, Materials (Basel) 12 (2) (2019).